Article

Current Biology

Activity-Dependent Actin Remodeling at the Base of Dendritic Spines Promotes Microtubule Entry

Graphical Abstract

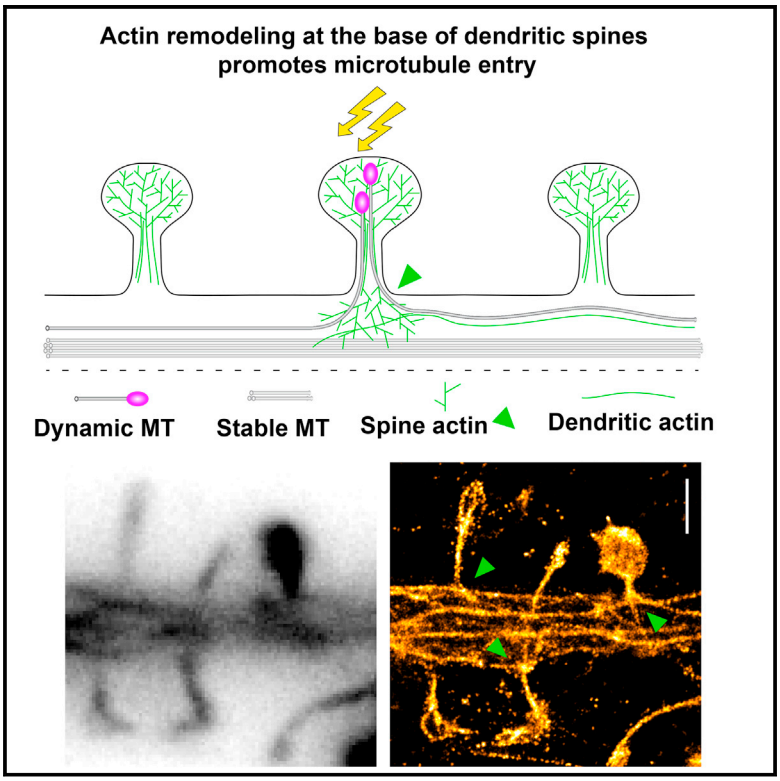

Highlights

- Spines are hotspots of microtubule catastrophes in mature dendrites
- NMDA receptor activation and calcium influx promote microtubule spine entry
- Actin remodeling at the base of the spine enables microtubule entry
- Local actin remodeling links synaptic activity to microtubule targeting

Authors

Philipp Schätzle,
Marta Esteves da Silva,
Roderick P. Tas, ...,
Corette J. Wierenga, Lukas C. Kapitein,
Casper C. Hoogenraad

Correspondence

c.hoogenraad@uu.nl

In Brief

Schätzle et al. identify a mechanism by which synaptic activity regulates microtubule entry into dendritic spines. Microtubules preferentially target spines that are undergoing actin reorganization in an activity-regulated manner. The authors show that structural changes in the actin cytoskeleton at the base of the spine promote microtubule entry.

Schätzle et al., 2018, Current Biology *28*, 2081–2093
July 9, 2018
https://doi.org/10.1016/j.cub.2018.05.004

CellPress

Current Biology
Article

Activity-Dependent Actin Remodeling at the Base of Dendritic Spines Promotes Microtubule Entry

Philipp Schätzle,[1] Marta Esteves da Silva,[1] Roderick P. Tas,[1] Eugene A. Katrukha,[1] Hai Yin Hu,[1] Corette J. Wierenga,[1] Lukas C. Kapitein,[1] and Casper C. Hoogenraad[1,2,*]
[1]Cell Biology, Department of Biology, Faculty of Science, Utrecht University, 3584 Utrecht, the Netherlands
[2]Lead Contact
*Correspondence: c.hoogenraad@uu.nl
https://doi.org/10.1016/j.cub.2018.05.004

SUMMARY

In neurons, microtubules form dense bundles and run along the length of axons and dendrites. Occasionally, dendritic microtubules can grow from the shaft directly into dendritic spines. Microtubules target dendritic spines that are undergoing activity-dependent changes, but the mechanism by which microtubules enter spines has remained poorly understood. Using live-cell imaging, high-resolution microscopy, and local glutamate uncaging, we show that local actin remodeling at the base of a spine promotes microtubule spine targeting. Microtubule spine entry is triggered by activation of *N*-Methyl-D-aspartic acid (NMDA) receptors and calcium influx and requires dynamic actin remodeling. Activity-dependent translocation of the actin remodeling protein cortactin out of the spine correlates with increased microtubule targeting at a single spine level. Our data show that the structural changes in the actin cytoskeleton at the base of the spine are directly involved in microtubule entry and emphasize the importance of actin-microtubule crosstalk in orchestrating synapse function and plasticity.

INTRODUCTION

Microtubules are critical structures for stable neuronal morphology. They can serve as tracks for cargo transport, provide dynamic and mechanical functions, and control local signaling events [1]. In dendrites, microtubules polymerize from their plus ends along the length of the dendrite in both anterograde and retrograde directions [2]. Equal numbers of opposing microtubule orientations throughout the dendritic processes have been reported *in vitro* and *in vivo* [3]. Occasionally, microtubules can polymerize from the dendritic shaft directly into dendritic spines [4, 5]. Even though microtubules enter spines spontaneously, subsequent studies have shown that these microtubule invasions of spines are regulated by synaptic activity. Recent work has shown that microtubule invasion frequency increases after induction of chemical long-term potentiation (cLTP) [6]. In contrast, applying a paradigm that induces chemical long-term depression (cLTD) results in a loss of microtubule dynamics in dendritic spines [7]. However, the mechanistic link between neuronal activity and microtubule entry into spines remains largely unclear.

Dynamic microtubule entry in dendritic spines has been thought to contribute to processes related to synaptic maintenance and plasticity. For instance, recent data showed that microtubules entering dendritic spines provide a direct route for microtubule-based, motor-driven transport of selective synaptic cargo into spines [8]. Under basal conditions, the frequency of microtubule-spine invasions is relatively low, making actin-based transport a more generic way of driving cargo trafficking in spines. For example, it has been shown that endoplasmic reticulum and recycling endosomes use myosin V motors to enter spines [9–11]. However, kinesin-3 family proteins (KIF1A and KIF1C) can act as microtubule-base motors that transport cargo along newly polymerized microtubules directly into spines [8, 12]. The mechanism by which microtubules enter dendritic spines has remained poorly understood. In this study, we investigate which processes regulate microtubule entry into spines.

RESULTS

Microtubules Enter Dendritic Spines in Cultured Neurons and Organotypic Slices

The invasion of dendritic spines by dynamic microtubules was recently shown in developing neuron culture systems [4–6, 13]. Using a lentivirus-based inducible expression system, we demonstrate microtubule entry in spines in mature rat dissociated hippocampal neuron cultures (up to day *in vitro* 45 [DIV45]) and in dentate gyrus granule cells of organotypic mouse hippocampal slice cultures (Figure 1A). We observed frequent microtubule invasions in spines in both culture types and at different stages of maturation, indicating that this phenomenon is not limited to a transient phase during development (Figure 1B). The average spine entry frequency in slices was about half of the observed value for dissociated neuron cultures (Figure 1B), which is partially explained by a higher spine density compared to the number of dynamic microtubules in granule cells (Figures 1C and 1D). We found that microtubules grew over remarkable distances before entering a spine (Figure 1E). This was even more pronounced in slice cultures, where 25% of all spine entries were preceded by growth episodes of 20–50 μm. Furthermore, a considerable number of comet traces crossed the acquisition borders in time and/or space, which means that the actual length of many comets was actually underestimated. This observation is

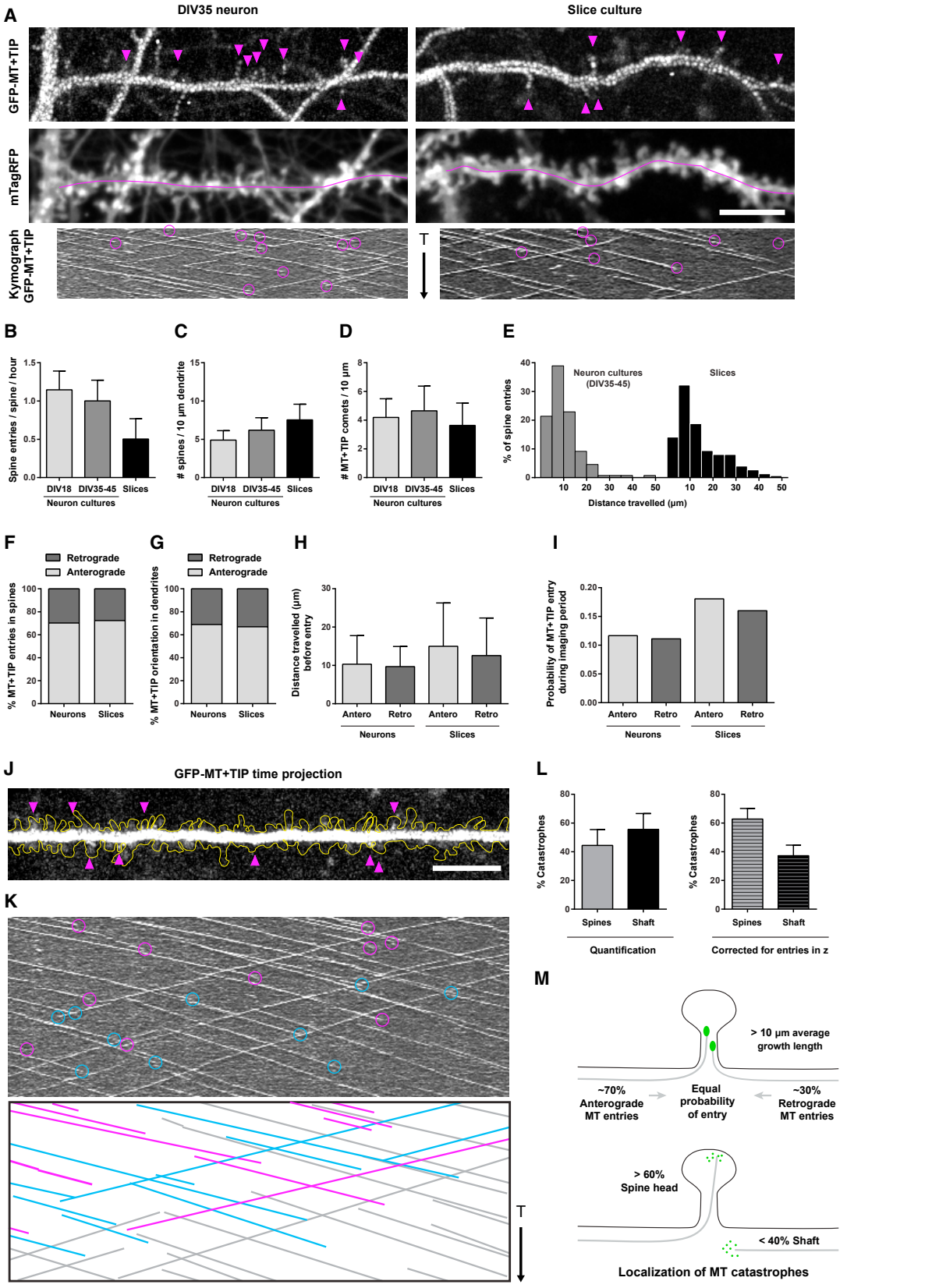

(legend on next page)

in conflict with a recent publication where it is reported that microtubules travel short distances before spine invasions [14]. This discrepancy could be explained by the limited z-resolution of total internal reflection fluorescence (TIRF) microscopy used in the aforementioned study. The bidirectional polarity of growing microtubules in dendrites [3] could entail that one orientation is preferential for spine entries. However, the polarity of microtubules entering spines (Figure 1F) was identical to the orientation of the total dynamic microtubule population (Figure 1G). Consistently, microtubules of opposed polarity did not show differences for the covered distances before spine entries (Figure 1H) and spine entry probabilities (Figure 1I). These data demonstrate that the polarity of microtubules is not a determinant factor for the targeting of dendritic spines (Figure 1M).

Spines Are Hotspots of Microtubule Catastrophes in Mature Dendrites

The growth and shrinkage of microtubules is controlled by a variety of regulatory proteins that interact with the plus-tip or the microtubule lattice [15]. In slice cultures, the majority of microtubule catastrophes were not followed by a microtubule rescue event (see, for instance, the kymograph in Figure 1K). As spine entries always result in a microtubule catastrophe, we asked to which extent this scenario accounts for the termination of microtubule growth in the dendrite. Based on kymographs, we identified microtubule catastrophes in slices and analyzed whether these occur within the dendrite or in spines (Figures 1J and 1K). Surprisingly, more than 40% of the microtubule catastrophes could directly be associated with entries in spines (magenta circles in Figure 1K). However, this number reflects only spine entries identified in x,y dimensions because we limited imaging to a few z-planes to capture the rapid dynamics. We therefore applied a z-correction factor that was determined by the assumption that spine entries cannot be resolved if the spine is more than ±60 degrees out of the imaging plane. This correction increased the proportion of catastrophes occurring in spines to more than 60% (Figure 1L), suggesting that spine entries may represent the default pathway of terminating the growth of dynamic microtubules in mature neurons.

Increasing Dendritic Calcium Levels Increase Microtubule Entries in Spines

Previous studies in dissociated neurons suggest a regulatory effect of synaptic activation on spine invasions by microtubules [6, 7, 14]. To verify this in slices, we applied pharmacological treatments that modulate the pattern of synaptic activation in hippocampal slice cultures and analyzed microtubule dynamics in spines. Although decreasing (tetrodotoxin [TTX]) or increasing (picrotoxin [PTX]) network activity did not affect spine entry frequencies in slices, we observed a small but significant decrease using low concentrations of 3,5-Dihydroxyphenylglycine (DHPG), known to induce chemical LTD in slices (Figure 2A). The most striking effect was found after application of the muscarinic agonist methacholine (MCh). Cholinergic stimulation has been used by several groups to induce LTP in hippocampal slice cultures and acute slices via G-protein-coupled release of calcium from inositol triphosphate (IP_3)-sensitive stores [16, 17]. Following methacholine stimulation, we observed a doubling of spine entry events compared to control conditions (Figures 2A–2C; Video S1). Interestingly, TTX-induced blocking of action potentials did not abolish the potentiating effect of methacholine, suggesting that the MCh-induced increase of intracellular calcium is sufficient to increase microtubule invasions in spines (Figures 2A and 2C). We did not observe a significant change in microtubule dynamics and density as a result of the MCh stimulation protocol (Figures 2D and 2E). Our data are in agreement with a recent study demonstrating an increase of microtubule invasions in spines of dissociated cultures after

Figure 1. Microtubules Invade Spines in Mature Cultured Neuron and Organotypic Slice

(A) Dendrites from lentiviral-transduced hippocampal dissociated neurons (rat) and dentate gyrus granule cells of a hippocampal slice culture (mouse) expressing a marker for dynamic microtubules (MT+TIP, top) and cellular morphology (mTagRFP, middle). The top panel shows maximum projections of average-subtracted time-lapse recordings of MT+TIP comets (6 min). Arrowheads highlight examples of microtubules entering spines. The middle panel shows average projections of the full time lapse, and the line displays the dendritic sections used for kymographs. Bottom panels show kymographs of the MT+TIP comets from the top panels. Magenta circles indicate microtubules invading spines.

(B) Quantification of spine entry frequency in cultured neurons and slice cultures. Cultured neurons DIV18: n = 10; DIV35–45: n = 25; slices: n = 37 analyzed neurons.

(C) Quantification of spine number per 10 μm dendrite (n = identical to B).

(D) Density of MT+TIP comets per 10 μm dendrite.

(E) Histogram of distance traveled by MT+TIP comets entering a spine in neuron (left graph) and slice cultures (right graph). Bin size = 5 μm; neurons: n = 131 comets; slices: n = 149 comets.

(F) Orientation of microtubules invading spines (n = identical to E).

(G) Distribution of anterograde- and retrograde-oriented MT+TIP comets in neurons and slice cultures. DIV35–45: n = 1,140 comets; slices: n = 859 comets.

(H) Average distance MT+TIP comets traveled before entering a spine.

(I) Probability of MT+TIP comets entering a spine relative to its orientation (pooled data).

(D)–(I) make use of the same dataset. Cultured neurons DIV18: n = 14 dendrites from 2 preparations; DIV35–45: n = 25 dendrites from 2 preparations; slices: n = 21 dendrites from 6 preparations.

(J) Maximum intensity projection of MT+TIP comets time-lapse recording in slices. The spine outline was generated from mTagRFP signal. Arrowheads indicate microtubule entries in spines.

(K) Kymograph of the MT+TIP comets shown in (J). Microtubule catastrophes within spines are highlighted by magenta circles and catastrophes without detectable spine entries (shaft) by cyan circles. Bottom graph shows a drawing of the kymograph using the same color code. Gray lines represent microtubule traces without observable catastrophes. The scale and time lapse length are identical to (J).

(L) Localization of microtubule catastrophes in dendrites of slice cultures. Right graph is corrected for false positive shaft catastrophes resulting from limited z-resolution. n = 203 comets of 12 dendrites from 10 slices of 4 preparations.

(M) Summary of findings: spine targeting is not selective for microtubule polarity, but the higher number of anterograde growing microtubules results in a more frequent targeting of this orientation. Spines represent preferred localizations for microtubule growth termination.

The scale bars represent 10 μm. Vertical arrows, 4 min. Bars diagrams show mean + SD.

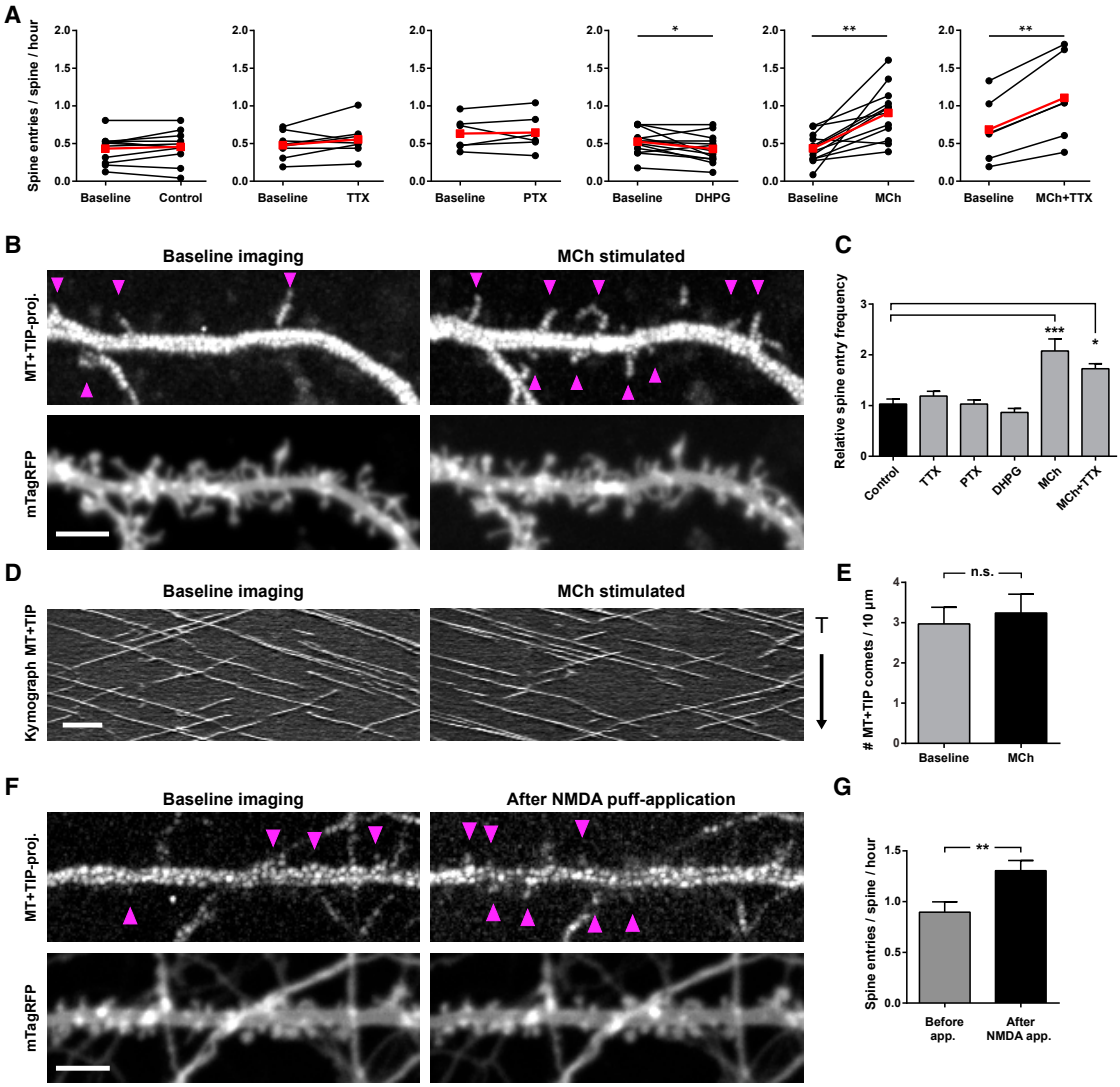

Figure 2. Specific Synaptic Activation Modulates Microtubule Invasions in Spines

(A) Synaptic activation in slice cultures was altered by indicated pharmacological treatments. Cultures were transduced with lentivirus expressing GFP-tagged MT+TIP marker and mTagRFP. Red points represent the mean values of the dataset. *p < 0.05; **p < 0.01; paired t test; control: n = 11; TTX: n = 8; PTX: n = 6; DHPG: n = 13; methacholine (MCh): n = 12; MCh+TTX: n = 6 dendrites.

(B) Example of MCh-stimulated dendrite showing projections of MT+TIP comets (upper panel) and dendrite morphology (lower panel) before and after stimulation in slice cultures. Arrowheads indicate examples of MT-+TIP entries in spines. See also Video S1.

(C) Relative change of spine entry frequency in slice cultures (frequency stimulation divided by baseline frequency) for each treatment in (A). *p < 0.05; ***p < 0.0001; one-way ANOVA with post hoc Dunnett's test.

(D) Kymographs of the MT+TIP comets shown in (B) before and after MCh stimulation (both 8:15 min recordings).

(E) Quantification of MT+TIP comet density per 10 μm dendrite in slice cultures. n.s., not significant; paired t test; n = 15 dendrites.

(F) Neuron culture infected with virus expressing MT+TIP marker and mTagRFP. Dendrite recorded 4 min before and after local puff application of NMDA. Panels are arranged as in (B).

(G) Quantification of spine entry frequency before and after local NMDA application. **p < 0.01, paired t test; n = 12 dendrites.

The scale bars represent 5 μm. Bars diagrams show mean + SEM. See also Video S1.

stimulation with a glycine-based chemical LTP protocol [14]. To confirm the role of dendritic calcium levels in this process, we applied brief local application of *N*-Methyl-D-aspartic acid (NMDA) on TTX-silenced neuron cultures (Figure 2F). Quantifications of spine entry frequencies before and after application revealed a significant increase following NMDA-induced increase in calcium levels (Figure 2G). Together, these experiments suggest that intracellular calcium is involved in the regulation of spine targeting by microtubules.

Regulation of Spine Targeting on the Level of Single Synapses

To our knowledge, all previous studies addressing the effects of synaptic activity on microtubule dynamics in spines were

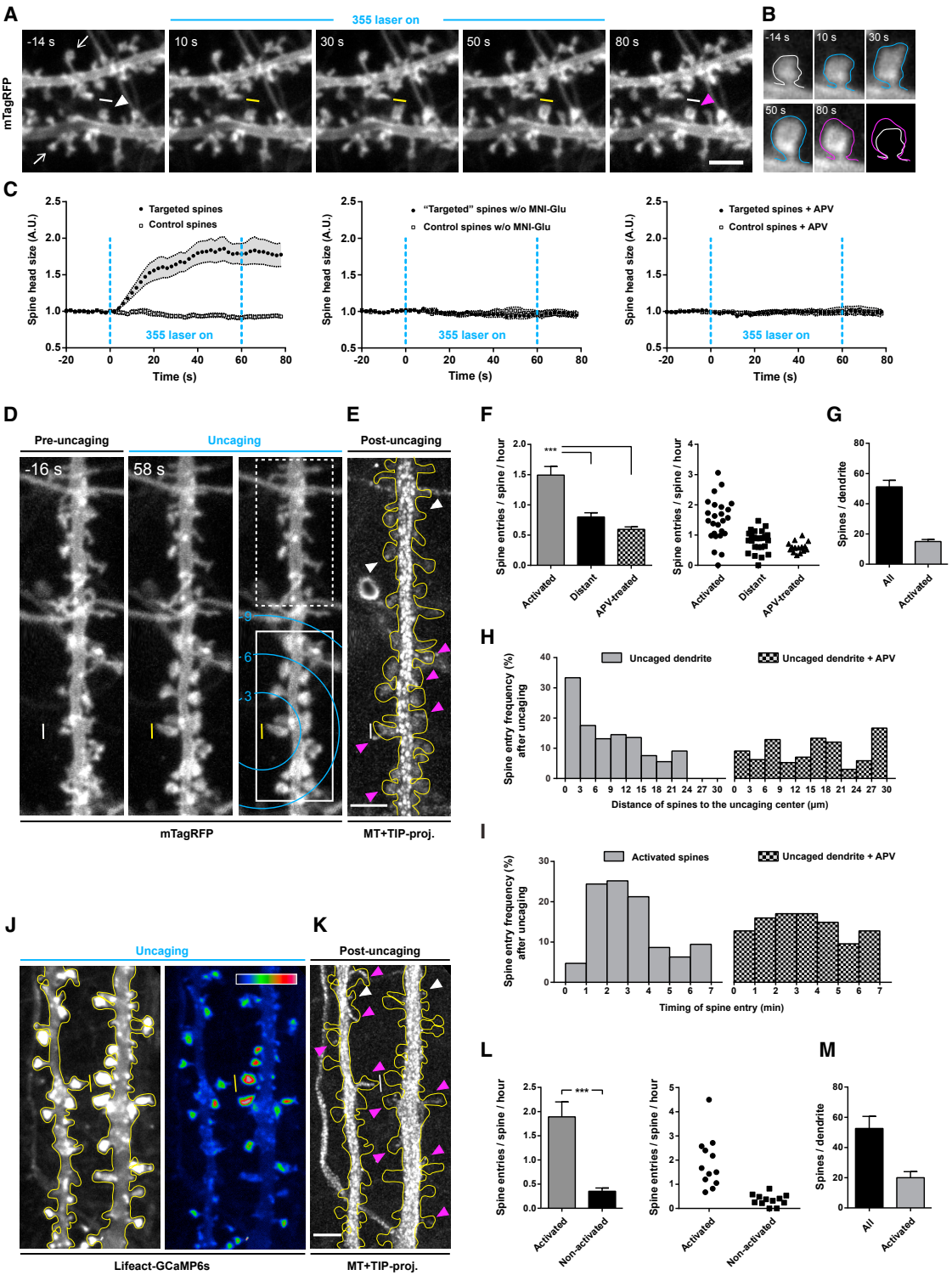

Figure 3. NMDA Receptor Activation Triggers Microtubule Entry in Spines

(A) Still frames of a dissociated neuron expressing mTagRFP. The first and last images represent time points before and after single-photon glutamate uncaging. Uncaging intervals were 0.5 Hz starting from 0 s for 1 min. The white or yellow line marks the uncaging spot; arrowhead indicates a targeted spine, and the arrows point to examples of spines that do not respond by size changes.

(B) The targeted spine in (A) at higher magnification. Spine outline was traced, and the last image shows an overlay of the before and after uncaging situation.

(C) Quantification of the change in spine head size in response to the uncaging stimulus over time. Targeted spines lay in close proximity to the uncaging spot, and control spines were chosen with a maximum possible distance to this position. Left graph shows the results of the standard uncaging protocol (targeted: n = 21;

(legend continued on next page)

performed using global stimulation protocols. The above-described local NMDA applications were our first attempts to target individual synapses. However, recordings of calcium dynamics showed that the majority of synapses within the field of view became activated, and NMDA stimulation evoked calcium waves extending throughout the dendrite. To activate only a small population of synapses along a dendrite, we performed glutamate uncaging on cultured neurons. Two-photon uncaging in slice cultures is associated with an NMDA-dependent increase in spine size [18, 19]. We used spine growth as readout of successful single-photon glutamate uncaging in our neuronal cultures. Spines close to the uncaging region showed an almost 2-fold increase in size, whereas distant control spines were unchanged (Figures 3A–3D). Additional control experiments demonstrated that the spine size changes were not a direct result of the 355 nm laser excitation but depended on the activation of NMDA receptors (Figure 3C). Next, we combined the uncaging protocol with subsequent recording of microtubule dynamics (Figures 3D and 3E; Video S2). Quantifications of microtubule invasions showed that the microtubule (MT) entry frequency on activated spines was almost two-fold increased when compared to distant spines (Figure 3F). Uncaging in the presence of 2-Amino-5-phosphonopentanoic acid (APV) resulted in a lower invasion frequency, which was similar to distant spines. As an alternative quantification, we determined the spine entry frequency relative to the distance to the uncaging center, which confirmed that spines in close proximity to the uncaging region were more frequently targeted than more distant spines (Figure 3H). This effect was absent when APV was applied. The spine-entry-promoting effect could be observed starting from 1 min after the end of the uncaging stimulus and lasted for about 3 min (Figure 3I). Although these uncaging experiments strongly suggest that local activation induces local targeting, our approach could not indisputably resolve the activation state of individual spines. To overcome this, we combined the uncaging experiments with a readout of the NMDA-evoked calcium transients. A fusion construct of Lifeact and GCaMP6s resulted in a highly specific indicator for calcium signals in spines. The combined recording of calcium signals and microtubule dynamics (Figures 3J and 3K; Video S3) showed a strong correlation between activated spines and microtubule targeting events in the uncaging experiments (Figure 3L). Both approaches to identify activated spines showed similar numbers (Figures 3G and 3M). In summary, the activation of a small number of dendritic spines using glutamate uncaging yielded direct evidence for a coupling between synaptic activation and increased probability of targeting by dynamic microtubules on the level of single spines.

Microtubule Targeting in Spines Depends on Actin Remodeling

The actin cytoskeleton in spines is a major downstream target of activity-induced plastic changes at synapses [20]. To determine whether actin plays a role in microtubule entries in spines, we pharmacologically interfered with actin dynamics. We monitored spine size and actin in neuron cultures expressing the actin marker Lifeact in control conditions and after incubation with the actin-stabilizing drug jasplakinolide. The treatment did not increase spine size but reduced actin-based motility of the spine heads [21] (Figure 4A). Interestingly, microtubule entries in spines were strongly increased by jasplakinolide, whereas the total number of comets remained stable but the relative comet density decreased (Figures 4A, 4B, and S2A–S2C). In contrast, disruption of actin structures with latrunculin B induced a significant decrease of spine entry frequency in dissociated neurons (Figure 4B). We found similar results in slice cultures, in which jasplakinolide also increased spine entry frequency (Figure 4C). Remarkably, the methacholine-induced potentiating effect on spine entry in slices (Figure 2A) was completely abolished in the presence of latrunculin B (Figure 4C). These data demonstrate a clear involvement of actin in the microtubule invasion of spines.

control: n = 26 spines). Middle graph represents a control condition in which the light pulse is applied in the absence of caged glutamate (targeted: n = 9; control: n = 9 spines) and right graph shows the uncaging experiment in the presence of the NMDA receptor blocker APV (targeted: n = 10; control: n = 11 spines). Error bars indicate SEM.

(D) Dendrite morphology before (left) and during glutamate uncaging (middle). Based on the morphological response to the stimulation, spines were classified as "activated" (white box) and "non-activated" (dashed box). White or yellow line marks the uncaging spot, and the circles indicate the distance to the center of the uncaging region. See also Video S2.

(E) Maximum projection of the MT+TIP comets time lapse recorded after the uncaging session. Magenta arrowheads show MT-+TIP spine entries in activated spines and white arrowheads in a non-activated spine. See also Video S2.

(F) Quantification of spine entries following glutamate uncaging. Entry frequencies for activated and non-activated distant spines are shown separately, whereas this separation was not made for APV experiments. Right graph shows the individual experiments, where each point represents the mean spine entry frequency of an uncaged dendrite. ***$p < 0.0001$; one-way ANOVA with post hoc Tukey's test; uncaged: n = 25; APV silenced: n = 17 dendrites.

(G) Average spine numbers of the analyzed experiments and the fraction considered activated.

(H) Histogram showing the relative frequency of spine entries in relation to the localization of spines to the uncaging region. Microtubule dynamics were recorded for 8 min after uncaging. Invaded and non-invaded spines were quantified together with their distance to the uncaging region. Data are presented in bins of 3-μm intervals for uncaged control and APV-treated dendrites (uncaged: n = 20; APV: n = 17 dendrites).

(I) Histogram showing the relative spine entries frequency relative to the time point of microtubule entry. Spines previously identified as activated are compared to APV silenced spines (activated: n = 39 dendrites with 153 entries; APV: n = 17 dendrites with 103 entries).

(J) Maximum projection of a Lifeact-GCaMP6s time lapse acquired during uncaging of glutamate. The levels are strongly enhanced to identify all spines on the dendrite (left). The color-coded sum projection allows the identification of activated spines (right). Yellow line marks the uncaging region; insert in top right corner shows lookup table for the color code. See also Video S3.

(K) Projection of MT+TIP comets time lapse recorded after the uncaging session. Microtubule entries in activated spines are highlighted with magenta arrowheads and entries in non-activated spines with white arrowheads. See also Video S3.

(L) Quantification of spine entry frequency following glutamate uncaging. Activated and non-activated spines are identified on their GCaMP6s signal. ***$p < 0.0001$; Mann-Whitney test; n = 12 dendrites. The scatterplot on the right shows the results of the individual experiments.

(M) Average total and activated spine numbers of the analyzed experiments.

The scale bars represent 3 μm. Bars diagrams show mean + SEM.

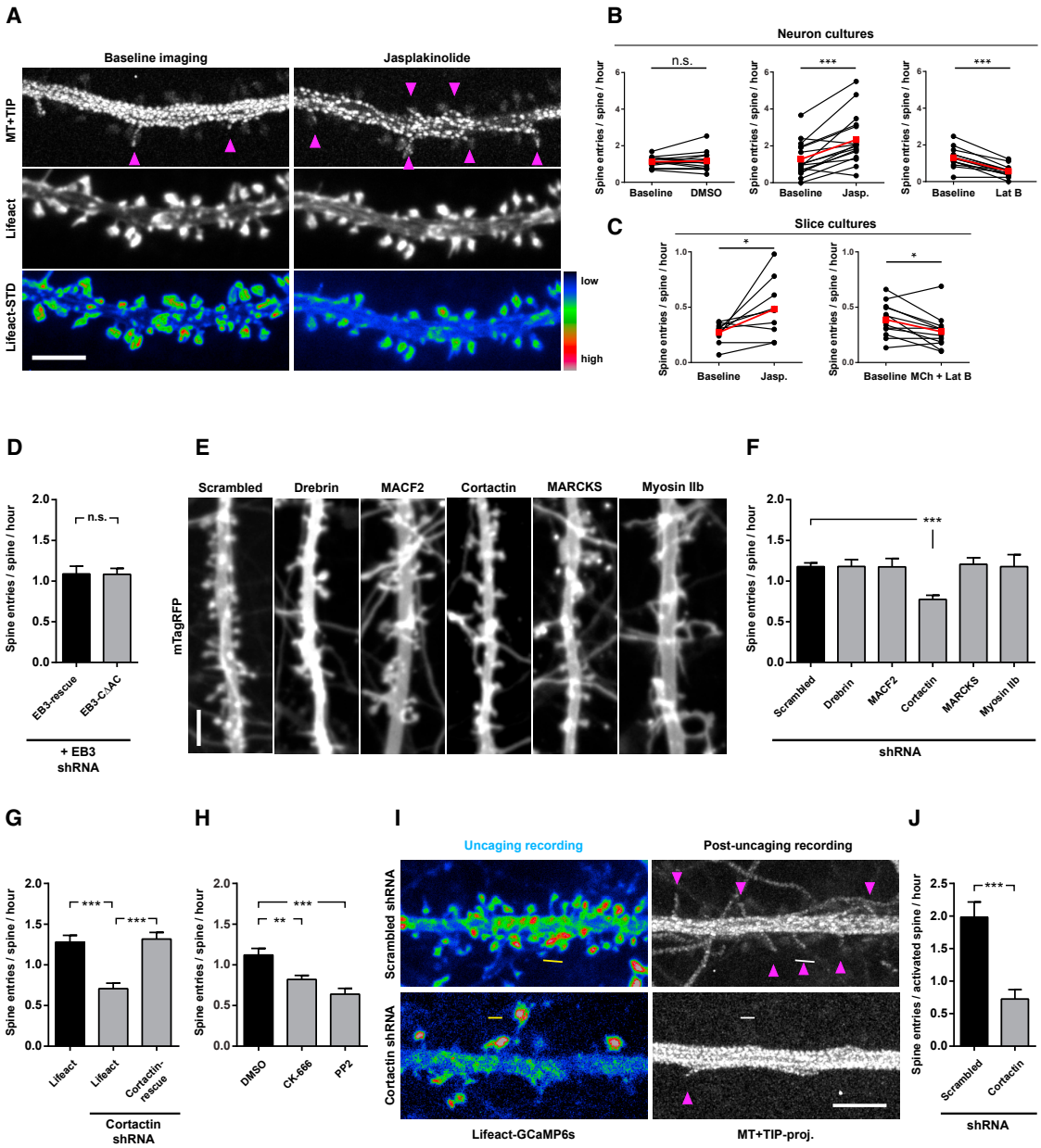

Figure 4. Actin Is Important for Mediating Microtubule Entries in Spines

(A) Dendrite of a dissociated neuron before and after treatment with jasplakinolide. Neurons were infected with virus co-expressing MT+TIP marker and Lifeact. Top panel shows the projection of the MT+TIP comets, middle panel is a still frame of the Lifeact signal, and bottom panel is a projection of the SD of the complete Lifeact time-lapse recording. Note that, following jasplakinolide treatment, there is a reduction in the number of MT+TIP comets and spine head dynamics but no increase in spine size.

(B) Effects on spine entry frequency in neuron cultures treated with DMSO (left) or actin-targeting drugs jasplakinolide (middle) and latrunculin B (right). Red points represent the mean values of the dataset. ***$p < 0.001$; paired t test; Jasp.: n = 16; Lat B: n = 14 dendrites.

(C) Slice culture experiments with either Jasp. (left) or a combination of MCh and Lat B (right). *$p < 0.05$; paired t test; Jasp.: n = 9; MCh+Lat B: n = 12 dendrites.

(D) Neuron cultures coinfected with EB3 shRNA virus and either the full-length GFP-EB3-rescue or GFP-EB3-CΔAC virus. Not significant; unpaired t test; EB3-rescue: n = 21; EB3-CΔAC: n = 22 dendrites.

(E) Representative examples of dendritic morphology after lentivirus-mediated depletion of the indicated target proteins in cultured neurons. Neurons were coinfected with virus expressing indicated shRNAs and virus expressing mTagRFP and the MT+TIP marker.

(F) Quantification of microtubule invasion frequencies in knockdown conditions. ***$p < 0.001$; one-way ANOVA with post hoc Dunnett's test; scrambled: n = 45; drebrin: n = 21; MACF2: n = 7; cortactin: n = 20; MARCKS: n = 15; Myosin IIb: n = 17 dendrites.

(G) Quantification of MT+TIP spine entries in baseline, cortactin-knockdown, or cortactin-rescue conditions. Neurons were depleted for endogenous cortactin with lentivirus and spines identified based on the Lifeact or the shRNA-resistant cortactin signals. ***$p < 0.0001$; one-way ANOVA with post hoc Tukey's test; Lifeact: n = 17; Lifeact+shRNA: n = 13; cortactin-rescue+shRNA: n = 14 dendrites.

(legend continued on next page)

The localization of endoplasmic reticulum (ER) in spines is another actin-dependent process [11] that is affected by synaptic activity [22], reminiscent of our microtubule spine invasions. As microtubule plus-tips can interact with the ER [23], we wondered whether growing microtubules were guided into spines by following previously established ER structures. To address this possibility, we overexpressed a dominant-negative myosin Va construct in dissociated neuron cultures to disrupt spine targeting of ER. Although we noticed a more than 5 times reduction of ER-positive spines in these experiments, there was no effect on the microtubule spine entry frequency (Figure S1), indicating that microtubule invasions occur independent of ER in spines.

End-binding proteins (EBs) recognize growing microtubule plus-tips and could be involved in the microtubule spine-targeting process through specific protein interactions via their acidic C-terminal tail region [15]. We therefore tested whether only disrupting these EB3 interactions would interfere with microtubule spine invasions. We observed full rescue of spine targeting after endogenous EB3 depletion and expression of EB3-CΔAC (Figure 4D), putting forward the idea that microtubule-actin interlinking proteins are not directly required in this process. Control experiments with co-expression of EB3 short hairpin RNA (shRNA) and the MT+TIP marker did not allow recording of microtubule comets, indicating strong depletion of endogenous EB3. Next, we investigated whether the knockdown of specific actin interacting and/or regulating proteins affects the targeting of spines by microtubules. Cortactin, myristoylated alanine-rich C-kinase substrate (MARCKS), and myosin IIb represent important regulators of actin dynamics in spines [24–26], whereas drebrin and microtubule actin cross-linking factor 2 (MACF2) were chosen due to their ability to directly interact with actin and growing microtubule plus-ends [27, 28]. Lentiviral-induced RNAi of the actin-interacting candidate proteins differentially affected spine morphology and density (Figures 4E and S2E). Interestingly, only the knockdown of cortactin resulted in a significant effect on microtubule spine entry frequency in dissociated neuron cultures (Figure 4F). To exclude potential off-target effects of the used cortactin-shRNA, we performed rescue experiments using a knockdown-resistant version of cortactin, which resulted in a comparable spine entry frequency as in control conditions (Figure 4G). Pharmacological blockade of the cortactin downstream target Arp2/3 complex (CK-666), as well as inhibition of upstream Src kinase (PP2), resulted in a significant decrease of spine targeting by microtubules (Figure 4H) [29]. The involvement of the actin regulator cortactin suggests that the actin cytoskeleton per se may facilitate microtubule spine targeting and that actin-microtubule interactions may be of less importance. An activity-dependent redistribution of cortactin and/or the underlying actin remodeling [24, 29, 30] may be linked to a role for cortactin in activity-dependent targeting of microtubules to spines. Using glutamate uncaging in combination with cortactin knockdown, we found a significant reduction of microtubule spine targeting, confirming the importance of cortactin-regulated actin dynamics in promoting spine entries (Figures 4I and 4J). Although overexpression of exogenous cortactin alters spine morphology, microtubule spine targeting and cortactin redistribution after glutamate uncaging is observed (Videos S4 and S5).

Actin Remodeling at the Base of the Spine

Actin dynamics have been extensively studied in the spine head but relatively little data exist about actin remodeling at the base of the spine. Electron microscopy has demonstrated a branched actin network at the base of the spine, which often overlapped with microtubules at the intersection between the spine neck and dendritic shaft [31]. We reasoned that the base of the spine is an important area for guiding microtubule entry into spines, and we analyzed actin dynamics at single spine level in greater detail. Glutamate uncaging-induced stimulation of spines in control neurons markedly increased actin fluorescence intensities (Lifeact) in spine heads and at the spine base (Figure 5A). Interestingly, the knockdown of cortactin significantly blocked the actin increase at the spine head and spine base in response to stimulation (Figures 5A–5C and S3; Video S6). These data suggest that the reduction of microtubule entries in spines observed after knockdown of cortactin (Figures 4E and 4F) may result from disturbed actin dynamics at the spine base. To test whether microtubule entries in spines correlate with actin dynamics at the base of the spine, we recorded actin dynamics in neuron cultures under baseline conditions. We frequently observed increased actin dynamics at the base of spines that were invaded by microtubules in the analyzed time lapses (Figures 5D and 5E; Video S6). Analysis of the signal intensities for actin and dynamic microtubules confirmed these observations (Figures 5F and 5G). Quantifications of the live-imaging data demonstrated that 77% of the invaded spines exhibit increased actin dynamics at the spine base (Figure 5H). Using the same quantification criteria, we found that 40% of all spines showed actin dynamics at the spine base (Figure 5I). By combining both quantifications, we found a significant association between microtubule entries and actin dynamics at the spine base (*$p < 0.001$; Fisher's exact test).

Consistent with the live-imaging data, single-molecule reconstructions of endogenous actin, using purified Lifeact, revealed actin structures and cables at the base of a subset of spines [32, 33] (Figure 6A). These structures could also be observed with direct stochastic optical reconstruction microscopy

(H) Quantification of MT+TIP spine entries in control conditions (DMSO) with Arp2/3 complex inhibitory drug CK-666, and Src inhibitory drug PP2. **$p < 0.01$; ***$p < 0.001$; one-way ANOVA with post hoc Dunnett's test; DMSO: n = 14; CK-666: n = 18; PP2: n = 15 dendrites.

(I) Glutamate uncaging experiment in control (upper) and cortactin-knockdown (lower) neuron cultures. Neuron cultures were coinfected with the cortactin-shRNA virus and virus expressing the MT+TIP marker and Lifeact-GCaMP6s. Left panel shows a sum projection of the Lifeact-GCaMP6s signal recorded during the glutamate uncaging protocol (yellow/white line marks uncaging region). The majority of spines within the field of view were activated because of a slightly stronger uncaging stimulation as in previous experiments (same color coding as in A). Right panel shows a projection of MT+TIP comets acquired after the uncaging session. Magenta arrowheads indicate microtubule entries in spines.

(J) Spine entry frequency after uncaging of glutamate for control and cortactin knockdown neurons. ***$p < 0.0001$; unpaired t test; scrambled: n = 15; cortactin: n = 16 dendrites.

The scale bars represent 5 μm. Bars diagrams show mean + SEM. See also Figures S1 and S2 and Videos S4 and S5.

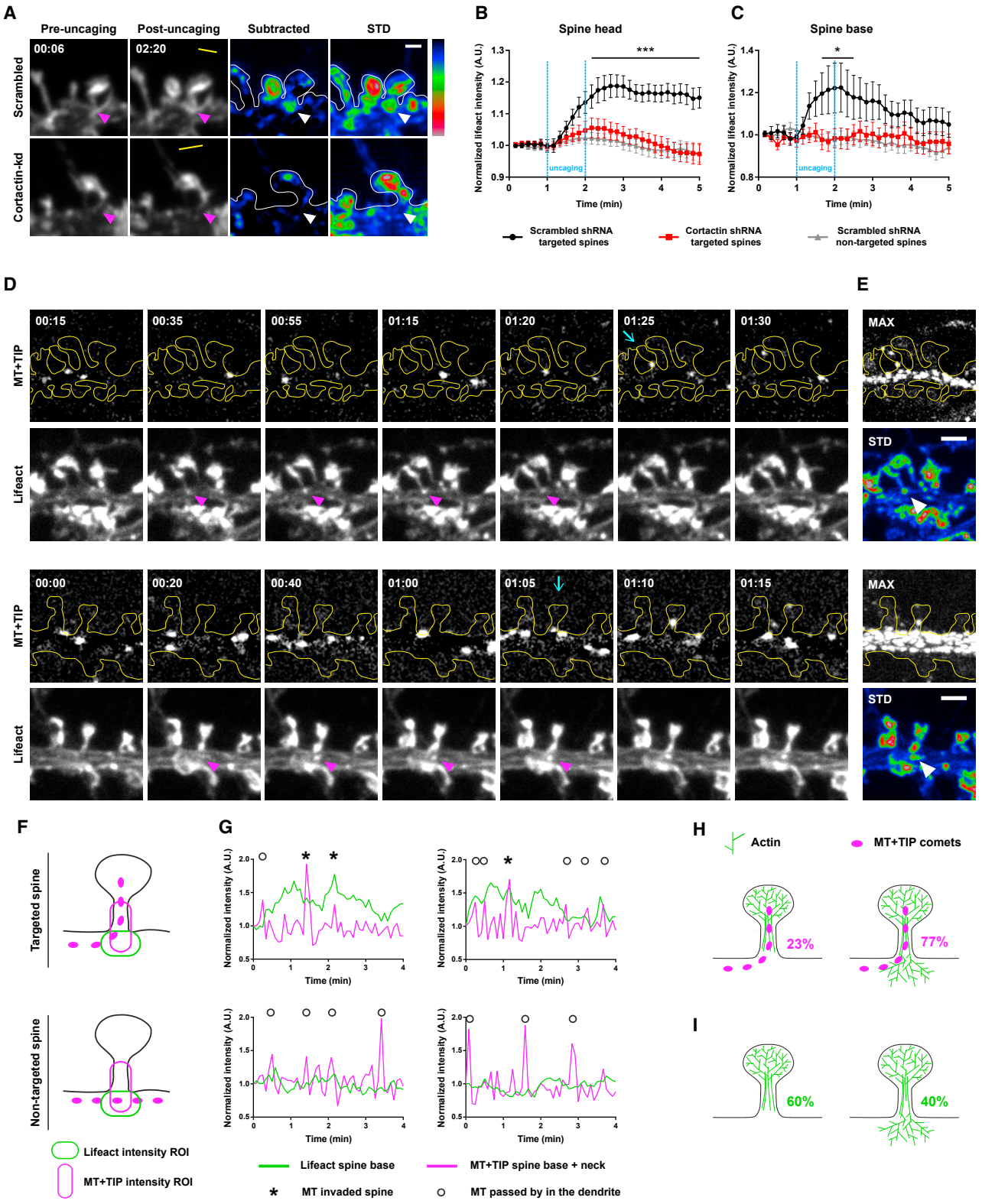

Figure 5. Actin Dynamics at the Spine Base

(A) Glutamate uncaging in neuron cultures expressing virus delivered Lifeact and either scrambled or cortactin shRNAs. First two columns show still frames before and after uncaging, and the yellow line indicates uncaging region. Next, subtraction of the pre- from the post-uncaging Lifeact signals to visualize the increases in

(legend continued on next page)

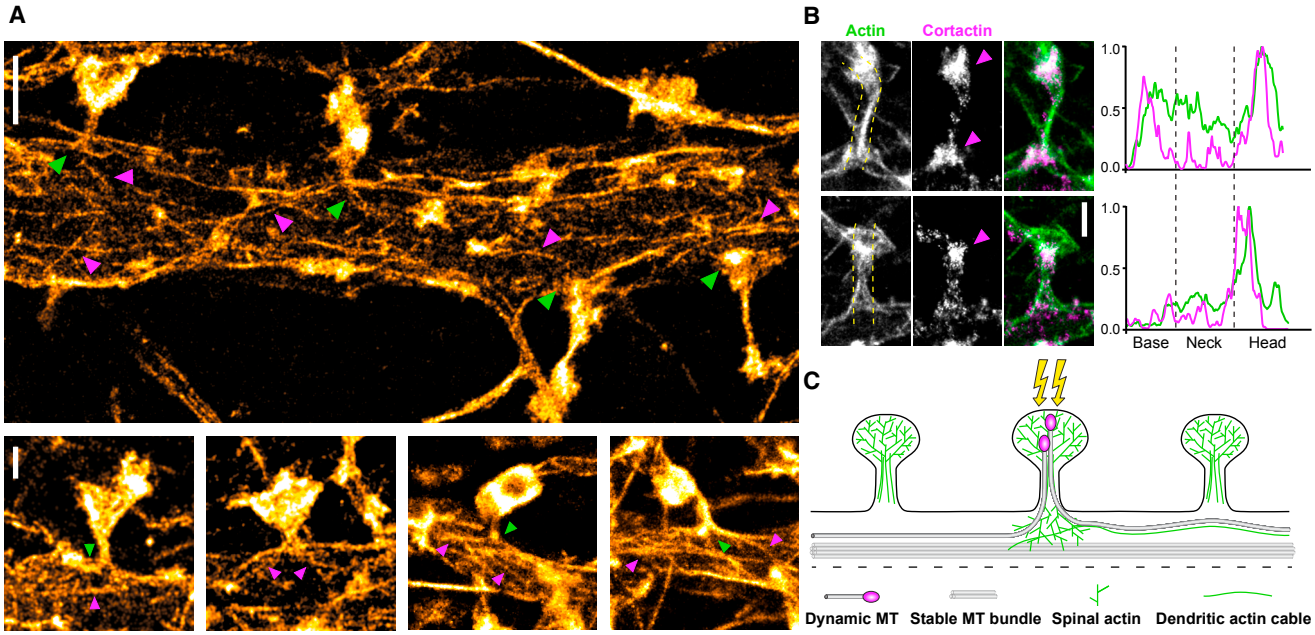

Figure 6. Super-resolution Imaging of Actin in Dendrites

(A) Untreated neuron cultures were fixed and imaged through transient binding of purified Lifeact-GFP or Lifeact-mNeonGreen. Regions of interest were identified through sparse labeling with phalloidin 568. Top panel shows a super-resolved reconstruction of the dendritic shaft and spines. Bottom panels show more examples of actin structures in individual spines. Green arrowheads indicate examples of actin structures at the spine base; magenta arrowheads indicate actin cables. The scale bars represent (overview) 1 μm and (zooms) 0.5 μm.

(B) 2-color super-resolution images of actin and cortactin in spines of DIV18+ neurons transfected with cortactin-dsRed. Magenta arrowheads indicate cortactin in the spine head or at the base. Corresponding line scans along both structures are shown for the area indicated in the middle panel. The scale bar represents 0.5 μm.

(C) Model illustrating potential mechanisms of microtubule entries in spines. Dynamic microtubules can interact with bundles of stable microtubules and/or dendritic actin cables. Synaptic stimulation enhances actin structures at the base of the spine, thereby connecting to stable microtubules and/or actin cables and leading to increased chances of microtubule targeting. See also Figure S4.

(dSTORM) imaging of labeled Lifeact-Myc after expression in neuronal cultures (Figure S4A). To further investigate whether cortactin can potentially influence actin dynamics by directly localizing to the spine base, two-color super resolution was performed. This revealed that expressed cortactin frequently colocalizes with the observed actin structures at the spine base and in the spine head (Figures 6B and S4B). Together, our results suggest that increasing the dynamics and remodeling of a specialized actin organization at the base of the spine enables microtubule entry into spines.

fluorescence intensity is shown. Right column is a projection of the Lifeact signal SD over the full 5 min recording to visualize hotspots of actin dynamics. Arrowheads point to the same position at the base of the spine. The scale bar represents 1 μm. Full-length recordings of these and additional examples are shown in Video S6.

(B) Quantification of Lifeact average intensities at the spine head in response to glutamate uncaging. Relative signals for activated spines in control or cortactin knockdown conditions and non-activated spines in control conditions are plotted over time. Data points represent mean ± SEM; ***$p < 0.001$; two-way ANOVA with post hoc Bonferroni test; scrambled activated: n = 20 spines; cortactin activated: n = 19 spines; scrambled non-activated: n = 22 spines. Spines from each condition were imaged from ≥15 dendrites of two independent cultures.

(C) Same dataset representation as in (B) showing quantified intensities for the corresponding spine bases. *$p < 0.05$; two-way ANOVA with post hoc Bonferroni test

(D) Still frames of two example neurons expressing MT+TIP and Lifeact. The moment of spine entries are indicated by a cyan arrow in the upper rows. Arrowheads indicate actin dynamics at the spine base. Note that time intervals change within the panel as indicated. Full time-lapse recordings of both examples can be found in Video S6.

(E) Maximum projection of the MT+TIP channel (upper) and a projection of the SD of the Lifeact signal to highlight actin dynamics (bottom). The scale bars represent 2 μm.

(F) Schematic representation of the regions of interest (ROIs) used in the quantification of actin and MT+TIP comets signals (left).

(G) Measurements of actin and MT+TIP signals of two targeted (examples from D) and two non-targeted spines. Curves represent the mean signal intensities measured in the ROIs at the spine base or spine base and neck. Asterisks indicate microtubules entering spines, and circles depict comets that passed by in the shaft.

(H) Manual quantification of actin dynamics in spines targeted by microtubules. Correlation was considered positive when actin dynamics at the spine base coincide in a window of 1 min before the microtubule enters the spine. In 21 dendrites, we analyzed 43 invaded spines, of which 33 showed actin dynamics at the spine base.

(I) The same dendrites were classified for actin dynamics independent of microtubule invasions. All spines were analyzed for actin dynamics at the spine base within the same 1 min time window as in the previous analysis. Spines: n = 217 positive and n = 323 negative for actin dynamics. See also Figure S3.

DISCUSSION

Here, we have identified a mechanism by which synaptic activity locally regulates microtubule entry into spines. We found that microtubule-spine entry is regulated by NMDA receptor activation and calcium influx and that actin remodeling is directly involved in microtubule entry. Our data demonstrate that structural changes in the actin cytoskeleton at the base of the spine allows for microtubule entry.

Microtubule Spine Entry Is Triggered by Activation of NMDA Receptor and Calcium Influx

We used a lentivirus-based inducible expression system of fluorescently labeled microtubule plus-ends combined with fast live-cell imaging to examine microtubule entry in dendritic spines in mature neurons in dissociated cultures and in organotypic hippocampal slices. Our findings demonstrate that microtubule entry into spines not only occurs in a transient episode during neuronal development but that it is very common and perhaps even the default pathway for terminating dendritic microtubule growth in adult neurons. We found that at least 40% of the microtubule catastrophes is directly associated with entries in spines under baseline conditions. Anterograde or retrograde growing microtubules did not show differences in spine entry probabilities, indicating that the polarity of microtubules in dendrites is not a determinant factor for the targeting of dendritic spines. Previous studies in dissociated neurons suggest a regulatory effect of synaptic activity on microtubule spine entry [6, 7, 14]. To investigate whether synaptic activity correlates with microtubule spine entry at the level of individual spines, we applied pharmacological treatments that modulate the pattern of synaptic activation in hippocampal slice cultures and analyzed microtubule dynamics in spines. We found that microtubule spine entry frequency was strongly increased following cLTP protocols that increase intracellular calcium levels. In addition, using glutamate uncaging in neuron cultures, we showed direct evidence for a coupling between NMDA-dependent synaptic activation and increased microtubule targeting on the level of single spines. Together, these data indicate that dynamic microtubules preferentially target dendritic spines that have recently experienced NMDA receptor (NMDAR)-mediated calcium increase.

Local Actin Remodeling Links Synaptic Activity and Microtubule Spine Entry

Calcium influx through NMDA receptors has been shown to alter the actin dynamics within dendritic spines [20]. Previous findings suggested that the microtubule plus-end binding protein EB3 through the interaction of microtubule actin-associated protein drebrin is involved in dendritic spine entries [14]. These conclusions are largely based on drebrin-overexpression experiments, where increased levels of drebrin promote microtubule invasion frequency and the number of spines invaded by microtubules [14]. Super-resolution microscopy imaging revealed that actin filaments at the spine base extend throughout the dendritic shaft. Consistent with microtubule-actin cooperation in various other cellular processes [34], it is possible that the actin filaments directly guide the entry of microtubules in dendritic spines. Our data also indicate that EB3 knockdown can be rescued by an EB3 construct lacking the C-terminal SxIP binding site. These results indicate that SxIP-mediated interactions between microtubule plus-ends and components of the actin cytoskeleton are not required for microtubule spine targeting. Therefore, we propose a model in which structural changes in the actin cytoskeleton at the base of the spine are through steric interactions rather than specific protein-protein interactions involved with microtubule entry (Figure 6C). In this way, activity-dependent remodeling of the actin cytoskeleton at the base of the spine may allow for regulated microtubule targeting. Obviously, actin-binding proteins remodeling the actin cytoskeleton are indirectly involved. An increase in actin dynamics at the spine base has also been observed using glutamate uncaging combined with actin photoactivation [35]. In approximately half of the stimulated spines, an outflow of actin and release of actin filaments from the spine head into the dendritic shaft was observed [35]. These data are consistent with an activity-dependent redistribution of cortactin [24, 29, 30] and the interpretation that local actin remodeling facilitates microtubule spine entries. Together, our data show that dynamic microtubules preferentially target spines that are undergoing actin reorganization in an activity-regulated manner.

STAR★METHODS

Detailed methods are provided in the online version of this paper and include the following:

- KEY RESOURCES TABLE
- CONTACT FOR REAGENT AND RESOURCE SHARING
- EXPERIMENTAL MODEL AND SUBJECT DETAILS
  - Animals
  - Primary neuron culture and viral transduction/transfection
  - Primary tissue culture
- METHOD DETAILS
  - DNA plasmids and lentivirus
  - LifeAct-GFP purification
  - Pharmacological treatments
  - Live-cell imaging
  - Super resolution imaging
  - Image analysis and quantification
- QUANTIFICATION AND STATISTICAL ANALYSIS

SUPPLEMENTAL INFORMATION

Supplemental Information includes four figures and six videos and can be found with this article online at https://doi.org/10.1016/j.cub.2018.05.004.

ACKNOWLEDGMENTS

P.S. was supported by postdoctoral fellowships from the Marie-Curie Program (grant 326425) and the Swiss National Science Foundation (PBZHP3_147307). M.E.d.S. is supported by Fundação para a Ciência e Tecnologia (FCT) (Portugal; grant SFRH/BD/68642/2010). This work was further supported by the Netherlands Organization for Scientific Research (NWO-ALW-VICI, C.C.H.; NWO ZonMW-VIDI, C.J.W. and H.Y.H.; and ALW-VIDI, L.C.K.), the Netherlands Organization for Health Research and Development (ZonMW-TOP, C.C.H.), and the European Research Council (ERC) (ERC-consolidator 617050, C.C.H. and ERC-Starting Grant 336291, L.C.K.).

AUTHOR CONTRIBUTIONS

P.S. designed and performed the live-cell imaging experiments and analyzed the data; M.E.d.S. performed lentiviral transduction of neuronal cultures and live-cell imaging experiments; R.P.T. purified Lifeact-GFP and Lifeact-mNeonGreen and performed super-resolution of actin structures in the dendrites under supervision of L.C.K.; E.A.K. wrote automated comet analysis routine; H.Y.H. assisted with the uncaging experiments; C.J.W. and L.C.K. provided critical input for experimental design and data analysis; and P.S. and C.C.H. wrote the manuscript with comments by all other authors. C.C.H. supervised the project and coordinated the study.

DECLARATION OF INTERESTS

The authors declare no competing interests.

Received: August 30, 2017
Revised: March 17, 2018
Accepted: May 2, 2018
Published: June 14, 2018

REFERENCES

1. Kapitein, L.C., and Hoogenraad, C.C. (2015). Building the neuronal microtubule cytoskeleton. Neuron *87*, 492–506.
2. Stepanova, T., Slemmer, J., Hoogenraad, C.C., Lansbergen, G., Dortland, B., De Zeeuw, C.I., Grosveld, F., van Cappellen, G., Akhmanova, A., and Galjart, N. (2003). Visualization of microtubule growth in cultured neurons via the use of EB3-GFP (end-binding protein 3-green fluorescent protein). J. Neurosci. *23*, 2655–2664.
3. Yau, K.W., Schätzle, P., Tortosa, E., Pagès, S., Holtmaat, A., Kapitein, L.C., and Hoogenraad, C.C. (2016). Dendrites in vitro and in vivo contain microtubules of opposite polarity and axon formation correlates with uniform plus-end-out microtubule orientation. J. Neurosci. *36*, 1071–1085.
4. Jaworski, J., Kapitein, L.C., Gouveia, S.M., Dortland, B.R., Wulf, P.S., Grigoriev, I., Camera, P., Spangler, S.A., Di Stefano, P., Demmers, J., et al. (2009). Dynamic microtubules regulate dendritic spine morphology and synaptic plasticity. Neuron *61*, 85–100.
5. Hu, X., Viesselmann, C., Nam, S., Merriam, E., and Dent, E.W. (2008). Activity-dependent dynamic microtubule invasion of dendritic spines. J. Neurosci. *28*, 13094–13105.
6. Merriam, E.B., Lumbard, D.C., Viesselmann, C., Ballweg, J., Stevenson, M., Pietila, L., Hu, X., and Dent, E.W. (2011). Dynamic microtubules promote synaptic NMDA receptor-dependent spine enlargement. PLoS ONE *6*, e27688.
7. Kapitein, L.C., Yau, K.W., Gouveia, S.M., van der Zwan, W.A., Wulf, P.S., Keijzer, N., Demmers, J., Jaworski, J., Akhmanova, A., and Hoogenraad, C.C. (2011). NMDA receptor activation suppresses microtubule growth and spine entry. J. Neurosci. *31*, 8194–8209.
8. Esteves da Silva, M., Adrian, M., Schätzle, P., Lipka, J., Watanabe, T., Cho, S., Futai, K., Wierenga, C.J., Kapitein, L.C., and Hoogenraad, C.C. (2015). Positioning of AMPA receptor-containing endosomes regulates synapse architecture. Cell Rep. *13*, 933–943.
9. Correia, S.S., Bassani, S., Brown, T.C., Lisé, M.F., Backos, D.S., El-Husseini, A., Passafaro, M., and Esteban, J.A. (2008). Motor protein-dependent transport of AMPA receptors into spines during long-term potentiation. Nat. Neurosci. *11*, 457–466.
10. Wang, Z., Edwards, J.G., Riley, N., Provance, D.W., Jr., Karcher, R., Li, X.D., Davison, I.G., Ikebe, M., Mercer, J.A., Kauer, J.A., and Ehlers, M.D. (2008). Myosin Vb mobilizes recycling endosomes and AMPA receptors for postsynaptic plasticity. Cell *135*, 535–548.
11. Wagner, W., Brenowitz, S.D., and Hammer, J.A., 3rd. (2011). Myosin-Va transports the endoplasmic reticulum into the dendritic spines of Purkinje neurons. Nat. Cell Biol. *13*, 40–48.
12. McVicker, D.P., Awe, A.M., Richters, K.E., Wilson, R.L., Cowdrey, D.A., Hu, X., Chapman, E.R., and Dent, E.W. (2016). Transport of a kinesin-cargo pair along microtubules into dendritic spines undergoing synaptic plasticity. Nat. Commun. *7*, 12741.
13. Hu, X., Ballo, L., Pietila, L., Viesselmann, C., Ballweg, J., Lumbard, D., Stevenson, M., Merriam, E., and Dent, E.W. (2011). BDNF-induced increase of PSD-95 in dendritic spines requires dynamic microtubule invasions. J. Neurosci. *31*, 15597–15603.
14. Merriam, E.B., Millette, M., Lumbard, D.C., Saengsawang, W., Fothergill, T., Hu, X., Ferhat, L., and Dent, E.W. (2013). Synaptic regulation of microtubule dynamics in dendritic spines by calcium, F-actin, and drebrin. J. Neurosci. *33*, 16471–16482.
15. Akhmanova, A., and Steinmetz, M.O. (2008). Tracking the ends: a dynamic protein network controls the fate of microtubule tips. Nat. Rev. Mol. Cell Biol. *9*, 309–322.
16. De Roo, M., Klauser, P., and Muller, D. (2008). LTP promotes a selective long-term stabilization and clustering of dendritic spines. PLoS Biol. *6*, e219.
17. Fernández de Sevilla, D., Núñez, A., Borde, M., Malinow, R., and Buño, W. (2008). Cholinergic-mediated IP3-receptor activation induces long-lasting synaptic enhancement in CA1 pyramidal neurons. J. Neurosci. *28*, 1469–1478.
18. Matsuzaki, M., Honkura, N., Ellis-Davies, G.C., and Kasai, H. (2004). Structural basis of long-term potentiation in single dendritic spines. Nature *429*, 761–766.
19. Ross, W.N. (2012). Understanding calcium waves and sparks in central neurons. Nat. Rev. Neurosci. *13*, 157–168.
20. Hotulainen, P., and Hoogenraad, C.C. (2010). Actin in dendritic spines: connecting dynamics to function. J. Cell Biol. *189*, 619–629.
21. Fischer, M., Kaech, S., Knutti, D., and Matus, A. (1998). Rapid actin-based plasticity in dendritic spines. Neuron *20*, 847–854.
22. Holbro, N., Grunditz, A., and Oertner, T.G. (2009). Differential distribution of endoplasmic reticulum controls metabotropic signaling and plasticity at hippocampal synapses. Proc. Natl. Acad. Sci. USA *106*, 15055–15060.
23. Grigoriev, I., Gouveia, S.M., van der Vaart, B., Demmers, J., Smyth, J.T., Honnappa, S., Splinter, D., Steinmetz, M.O., Putney, J.W., Jr., Hoogenraad, C.C., and Akhmanova, A. (2008). STIM1 is a MT-plus-end-tracking protein involved in remodeling of the ER. Curr. Biol. *18*, 177–182.
24. Hering, H., and Sheng, M. (2003). Activity-dependent redistribution and essential role of cortactin in dendritic spine morphogenesis. J. Neurosci. *23*, 11759–11769.
25. Calabrese, B., and Halpain, S. (2005). Essential role for the PKC target MARCKS in maintaining dendritic spine morphology. Neuron *48*, 77–90.
26. Rex, C.S., Gavin, C.F., Rubio, M.D., Kramar, E.A., Chen, L.Y., Jia, Y., Huganir, R.L., Muzyczka, N., Gall, C.M., Miller, C.A., et al. (2010). Myosin IIb regulates actin dynamics during synaptic plasticity and memory formation. Neuron *67*, 603–617.
27. Geraldo, S., Khanzada, U.K., Parsons, M., Chilton, J.K., and Gordon-Weeks, P.R. (2008). Targeting of the F-actin-binding protein drebrin by the microtubule plus-tip protein EB3 is required for neuritogenesis. Nat. Cell Biol. *10*, 1181–1189.
28. Leung, C.L., Sun, D., Zheng, M., Knowles, D.R., and Liem, R.K. (1999). Microtubule actin cross-linking factor (MACF): a hybrid of dystonin and dystrophin that can interact with the actin and microtubule cytoskeletons. J. Cell Biol. *147*, 1275–1286.
29. Iki, J., Inoue, A., Bito, H., and Okabe, S. (2005). Bi-directional regulation of postsynaptic cortactin distribution by BDNF and NMDA receptor activity. Eur. J. Neurosci. *22*, 2985–2994.
30. Seese, R.R., Babayan, A.H., Katz, A.M., Cox, C.D., Lauterborn, J.C., Lynch, G., and Gall, C.M. (2012). LTP induction translocates cortactin at distant synapses in wild-type but not Fmr1 knock-out mice. J. Neurosci. *32*, 7403–7413.
31. Korobova, F., and Svitkina, T. (2010). Molecular architecture of synaptic actin cytoskeleton in hippocampal neurons reveals a mechanism of dendritic spine morphogenesis. Mol. Biol. Cell *21*, 165–176.

32. Kiuchi, T., Higuchi, M., Takamura, A., Maruoka, M., and Watanabe, N. (2015). Multitarget super-resolution microscopy with high-density labeling by exchangeable probes. Nat. Methods *12*, 743–746.

33. Tas, R.P., Bos, T.G.A.A., and Kapitein, L.C. (2018). Purification and application of a small actin probe for single-molecule localization microscopy. Methods Mol. Biol. *1665*, 155–171.

34. Rodriguez, O.C., Schaefer, A.W., Mandato, C.A., Forscher, P., Bement, W.M., and Waterman-Storer, C.M. (2003). Conserved microtubule-actin interactions in cell movement and morphogenesis. Nat. Cell Biol. *5*, 599–609.

35. Honkura, N., Matsuzaki, M., Noguchi, J., Ellis-Davies, G.C., and Kasai, H. (2008). The subspine organization of actin fibers regulates the structure and plasticity of dendritic spines. Neuron *57*, 719–729.

36. Schätzle, P., Kapitein, L.C., and Hoogenraad, C.C. (2016). Live imaging of microtubule dynamics in organotypic hippocampal slice cultures. Methods Cell Biol. *131*, 107–126.

37. MacGillavry, H.D., Kerr, J.M., Kassner, J., Frost, N.A., and Blanpied, T.A. (2016). Shank-cortactin interactions control actin dynamics to maintain flexibility of neuronal spines and synapses. Eur. J. Neurosci. *43*, 179–193.

38. Komarova, Y., Lansbergen, G., Galjart, N., Grosveld, F., Borisy, G.G., and Akhmanova, A. (2005). EB1 and EB3 control CLIP dissociation from the ends of growing microtubules. Mol. Biol. Cell *16*, 5334–5345.

39. Mikhaylova, M., Cloin, B.M., Finan, K., van den Berg, R., Teeuw, J., Kijanka, M.M., Sokolowski, M., Katrukha, E.A., Maidorn, M., Opazo, F., et al. (2015). Resolving bundled microtubules using anti-tubulin nanobodies. Nat. Commun. *6*, 7933.

40. Riedl, J., Crevenna, A.H., Kessenbrock, K., Yu, J.H., Neukirchen, D., Bista, M., Bradke, F., Jenne, D., Holak, T.A., Werb, Z., et al. (2008). Lifeact: a versatile marker to visualize F-actin. Nat. Methods *5*, 605–607.

41. Szymczak-Workman, A.L., Vignali, K.M., and Vignali, D.A. (2012). Design and construction of 2A peptide-linked multicistronic vectors. Cold Spring Harb. Protoc. *2012*, 199–204.

42. Yau, K.W., van Beuningen, S.F., Cunha-Ferreira, I., Cloin, B.M., van Battum, E.Y., Will, L., Schätzle, P., Tas, R.P., van Krugten, J., Katrukha, E.A., et al. (2014). Microtubule minus-end binding protein CAMSAP2 controls axon specification and dendrite development. Neuron *82*, 1058–1073.

43. van Beuningen, S.F.B., Will, L., Harterink, M., Chazeau, A., van Battum, E.Y., Frias, C.P., Franker, M.A.M., Katrukha, E.A., Stucchi, R., Vocking, K., et al. (2015). TRIM46 controls neuronal polarity and axon specification by driving the formation of parallel microtubule arrays. Neuron *88*, 1208–1226.

STAR★METHODS

KEY RESOURCES TABLE

REAGENT or RESOURCE	SOURCE	IDENTIFIER
Antibodies		
mouse anti-myc (clone 9E10)	Santa Cruz	sc-40
mouse anti-myc (Ab-1)	Oncogene Research	AB-1
Alexa 647 Goat Anti-Mouse IgG (H+L)	Molecular Probes, Life Technologies	Cat#A21236, RRID: AB_141725
rabbit anti-RFP	Rockland	600-401-379
anti-rabbit-D2	Ultivue	N/A
rabbit anti-Cortactin	Santa Cruz	H-191:sc-11408
rabbit anti-Drebrin	Abcam	ab11068
Bacterial and Virus Strains		
Escherichia coli: DH10B	N/A	N/A
Escherichia coli: Stbl3	ThermoFisher	Cat# C737303
Escherichia coli: BL21DE3	N/A	N/A
pLVTHPS-mEBFP2-HA_shRNA	This paper	N/A
pSIN-TRE-MCS-Synapsin-rtTA2	[36]	N/A
pSIN-TRE-mTagRFP_IRES_GFP-MACF18-Synapsin-rtTA2	[36]	N/A
pSIN-TRE-mTagRFP_IRES_GFP-EB3-rescue-Synapsin-rtTA2	This paper	N/A
pSIN-TRE-mTagRFP_IRES_GFP-EB3-ΔAc-Synapsin-rtTA2	This paper	N/A
pSIN-TRE-Lifeact-TagRFP-Myc_IRES_GFP-MACF18-Synapsin-rtTA2	This paper	N/A
pSIN-TRE-Lifeact-GCaMP6s_IRES_Tomato-MACF18-Synapsin-rtTA2	This paper	N/A
pSIN-TRE-TagRFP-ER_IRES_GFP-MACF18-Synapsin-rtTA2	This paper	N/A
pSIN-TRE-Cortactin-dsRed_IRES_GFP-MACF18-Synapsin-rtTA2	This paper	N/A
pSIN-TRE-mEBFP2-HA_P2A_Myc-MyoVa-tail-Synapsin-rtTA2	This paper	N/A
Chemicals, Peptides, and Recombinant Proteins		
Lipofectamine 2000	ThermoFisher	Cat# 11668019
APV	Tocris	Cat# 0106
CK-666	Tocris	Cat# 3950
DHPG	Tocris	Cat# 0805
Jasplakinolide	Tocris	Cat# 2792
Latrunculin B	Santa Cruz	Cat# SC-203318
Methacholine	Sigma	Cat# A2251
MNI-Glutamate	Tocris	Cat# 1490
NMDA	Sigma	Cat# M3262
Picrotoxin (PTX)	Tocris	Cat# 1128
PP2	Tocris	Cat# 1407
Trolox	Sigma	Cat# 238813
Tetrodotoxin (TTX)	Abcam	Cat# ab120055
Experimental Models: Organisms/Strains		
Hippocampal neuron cultures from embryonic day 18 rat brains (Wistar)	N/A	N/A
Hippocampal organotypic slice cultures from P5-6 mice (C57BL/6)	N/A	N/A
Recombinant DNA		
p.MDG2	Dr. Didier Trono (EPFL)	addgene #12259
psPAX2	Dr. Didier Trono (EPFL)	addgene #12260
GW2_Lifeact-GFP	This paper	N/A
βactin_Cortactin-dsRed-exp	[37], subcloned and mutated for this paper	N/A

(*Continued on next page*)

Continued

REAGENT or RESOURCE	SOURCE	IDENTIFIER
pET28a_Lifeact-GFP	[33]	N/A
pET28a_Lifeact-mNeonGreen	This paper	N/A
shRNA targeting sequence: scrambled: GGTTTATATCGCGGTTATT	This paper	N/A
shRNA targeting sequence: Cortactin: GCACTGCTCACAAGTGGAC	[24]	N/A
shRNA targeting sequence: Drebrin: GAGAACCAGAAAGTGATGTAC	[27]	N/A
shRNA targeting sequence: EB3: ACTATGATGGAAAGGATTAC	[38]	N/A
shRNA targeting sequence: MACF2: GCCGTGGTCAGAGTTGCTGAT	This paper	N/A
shRNA targeting sequence: MARCKS: CTGTACCAGTCAGTAATTA	[25]	N/A
shRNA targeting sequence: MyosinIIb: GATCAAAGTTGGCCGAGAT	[26]	N/A
Software and Algorithms		
FIJI	http://fiji.sc/	N/A
DoM Utrecht	[39]	https://github.com/ekatrukha/DoM_Utrecht
KymoResliceWide	GitHub	https://github.com/ekatrukha/KymoResliceWide
Prism	GraphPad	N/A
MATLAB	MathWorks	N/A

CONTACT FOR REAGENT AND RESOURCE SHARING

Further information and requests for resources and reagents should be directed and will be fulfilled by the Lead Contact, Casper Hoogenraad (c.hoogenraad@uu.nl).

EXPERIMENTAL MODEL AND SUBJECT DETAILS

Animals

All experiments were approved by the DEC (Dutch Experimental Review Committee), performed in line with institutional guidelines of the University Utrecht and were conducted in agreement with Dutch law (Wet op de Dierproeven, 1996) and European regulations (Guideline 86/609/EEC). Female pregnant Wistar rats were delivered from Janvier, aged at least 10 weeks at the time of delivery. Female pregnant C57BL/6 mice were delivered from Janvier, aged at least 15 weeks at the time of delivery. Upon delivery, animals were kept at SPF facilities in a controlled 12ch light-dark cycle with a temperature of 22 ± 1°C and given access to food pellets and water *ad libitum*. The animals were housed in small groups in transparent plexiglass cages with wood-chip bedding and paper tissue for nest building.

Primary neuron culture and viral transduction/transfection

Hippocampal neuron cultures were prepared from embryonic day 18 rat brains [3] (Wistar, both genders). Cells were plated on coverslips coated with poly-L-lysine (37.5 mg/mL) and laminin (1.25 mg/mL) at a density of 100,000/well and cultured at 37°C in 5% CO_2. Cultures were fed weekly by replacing 1/3 of the medium with fresh Neurobasal medium (NB) supplemented with 2% B27, 0.5 mM glutamine, and 1% penicillin/streptomycin. Experiments were performed with mature rat neuron cultures ranging from DIV 25-45, except for the analysis of spine entry frequencies in DIV18 neurons. Lentiviral infections were carried out 8-14 days before experiments. Inducible expression systems were triggered 2-4 days prior imaging by application of 500 ng/mL doxycycline. All infections with shRNA containing virus were carried out 8-9 days before experiments. Dendrites in knockdown experiments were routinely checked for clear mEBFP2 signals, confirming the infection with shRNA virus, before starting the actual experiments. Transfections were only applied for Video S4. Briefly, 0.9 μg GW2_Lifeact-GFP and 0.9 μg βactin_Cortactin-dsRed-exp vector were mixed with 3.3 μL Lipofectamine 2000 (Invitrogen) and incubated for 30 min. The mixture was added to coverslips placed in fresh NB and incubated for 45 min. Finally, neurons were washed in NB and translocated back into the original culture medium.

Primary tissue culture

Hippocampal organotypic interface slice cultures were generated from P5-6 mice pups (C57BL/6, both genders). Dissected hippocampi were cut in 350 μm sections and positioned on FHLC membrane patches (Millipore, FHLC01300) laying on Millicell culture inserts (Millipore, PICM0RG50). Viral infection was carried out within 2 hr after platting. Slices were fed every 2-3 days with culture medium containing 47.75% MEM, 25% HBSS, 25% horse serum, 1.25% 1M HEPES, 1% 3M D-glucose, pH 7.2 and osmolality of 310-320 mOsm. Detailed information about slice preparation and viral transduction has been published recently [36]. Experiments were made with slices kept for 2-4 weeks in culture.

METHOD DETAILS

DNA plasmids and lentivirus

Fluorescently tagged constructs were generated for subsequent subcloning in a bicistronic expression cassette. Membrane-targeted TagRFP-T (mTagRFP, generated from N-terminal first 41 amino acids of MARCKS) and the microtubule plus-tip marker (MT+TIP) GFP-MACF18 have been described previously [36]. Tomato-MACF18 is identical to GFP-MAC18 except for the replacement of GFP by tandem dimer Tomato (also called MT+TIP). Lifeact-TagRFP-Myc was PCR generated by cloning the 17 amino acid (aa) Lifeact sequence [40] linked by a 7 aa linker (GDPPVAT) to the N terminus of TagRFP-T (Evrogen). The TagRFP-T stop codon was replaced by a 4 aa linker (SSGS) followed by the 10 aa Myc sequence. Lifeact-GCaMP6s was based on the pGP-CMV-GCaMP6s (addgene #40753) vector. The start codon within this construct was replaced by the Lifeact sequence by a PCR based strategy. The TagRFP-ER construct is composed of the 17 amino acid rat calreticulin signal sequence fused to the N-term of TagRFP-T and a C-terminally located ER retention signal (KDEL). GFP-EB3-ΔAc and GFP-EB3-rescue constructs are identical to our previous publication [4]. Membrane-targeted EBFP2-HA was generated with a cryptic splice site corrected version of EBFP2 containing a C-terminal HA-tag. Cortactin-dsRed [37] was made shRNA resistant by introducing silent mutations in the target sequence using a PCR based strategy (GCATTGCTCTCAGGTGGAT).

Lifeact-GFP for super-resolution microscopy was generated using a bacteria codon optimized Lifeact fragment that was N-terminally inserted by PCR into a pET28a vector containing an EcoRI/XhoI flanked GFP or mNeonGreen sequence. The full vector was amplified with the LifeAct fragment and the template was digested with DPN1. The resulting construct was transformed into competent bacteria and sequenced.

Bicistronic expression constructs were generated based on the attenuated IRES site, derived from pIRES (Clonetech). This design allows high expression of the coding sequence upstream of the IRES site and relative low expression of the inserted downstream construct. The following plasmids were generated by conventional cloning strategies: mTagRFP_IRES_GFP-MACF18, mTagRFP_IRES_GFP-EB3-rescue, mTagRFP_IRES_GFP-EB3-ΔAc, Lifeact-TagRFP-Myc_IRES_GFP-MACF18, Lifeact-GCaMP6s_IRES_Tomato-MACF18, TagRFP-ER_IRES_GFP-MACF18, Cortactin-dsRed_IRES_GFP-MACF18. Equal expression of two constructs was achieved in the mEBFP2-HA_P2A_Myc-MyoVa-tail construct by using the 2A sequence of the porcine teschovirus-1 [41].

Lentiviral transfer vectors are based on the pSIN-TRE-MCS-Synapsin-rtTA2 plasmid [36]. The bicistronic expression cassettes described above were subcloned in the multiple cloning site resulting in a TET-On inducible expression of the target proteins. Full sequence information of all constructs can be provided on request.

RNAi-induced knockdown of target genes by lentivirus was based on a modified pLVTHM (addgene #12247) transfer vector, named pLVTHPS-mEBFP2-HA_shRNA. The original EF-1α promotor and GFP sequences were replaced by a central polypurine tract/central termination sequence (cPPT/CTS), followed by a short 0.5kb Synapsin promoter and mEBFP2-HA. Individual shRNA sequences were subcloned from the original pSuper vectors via BamHI and ClaI sites. Following shRNA target sequences were used: scrambled GGTTTATATCGCGGTTATT, Cortactin GCACTGCTCACAAGTGGAC [24], Drebrin GAGAACCAGAAAGTGATGTAC [27], EB3 ACTATGATGGAAAGGATTAC [38], MACF2 GCCGTGGTCAGAGTTGCTGAT, MARCKS CTGTACCAGTCAGTAATTA [25], Myosin IIb GATCAAAGTTGGCCGAGAT [26].

Lentiviral particles were generated by transfecting the transfer plasmid together with the packaging plasmids p.MDG2 (addgene #12259) and psPAX2 (addgene #12260) in HEK293T cells. The supernatant was collected two days after transfection and concentrated using tangential flow filtration (Amicon Ultra spin filters, Millipore #UFC910024). Detailed information about the lentivirus production has been described elsewhere [36].

LifeAct-GFP purification

LifeAct-GFP-6xHis was purified using standard His-tag purification methods. *E. coli* BL21DE3 were induced at OD 0.6 for overnight expression at 20 degrees. After pelleting the cells were lysed through sonication in the presence of lysozyme and a protease inhibitor cocktail (Roche). The soluble fraction was filtered and bound to a His-Trap HP 1 mL column (GE healthcare). Elution was performed on an AKTAxpress (GE healthcare). After buffer exchange to PBS the pure protein sample was frozen in 10% glycerol.

Pharmacological treatments

The 1st control imaging session in neuron cultures was performed in the original culture medium. Jasplakinolide (10 μM) or latrunculin B (1 μM) were diluted in 100 μL preconditioned culture medium, transferred into the recording chamber and incubated for 30 min before the 2nd recording session was started. For Cortactin inhibition experiments, neurons were preincubated in either DMSO (1:1000) for 30 min or 3 hr, CK-666 (100 μM) for 30 min, or PP2 (25 μM) for 3 hr. Next, neurons were transferred to the recording chamber and imaged in the presence of the drug.

The 1st control recordings of organotypic slice cultures were acquired in ACSF composed of 126 mM NaCl, 3 mM KCl, 2.5 mM $CaCl_2$, 1.3 mM $MgCl_2$, 1.25 mM Na_2HPO_4, 26 mM $NaHCO_3$, 20 mM glucose, and 1 mM Trolox (Sigma, 238813). For slice experiments, all drugs were diluted in ACSF and applied as continuous perfusion of the imaging chamber using a peristaltic pump. Following application pattern have been used. Control application: 0.1% DMSO incubated for 30min before start of 2nd recording session; TTX: 1 μM tetrodotoxin incubated for 30 min before 2nd recording; PTX: 100 μM picrotoxin incubated for 30 min before 2nd recording; DHPG: 50 μM dihydroxyphenylglycine incubated for 5 min + 5 min washout with ACSF before 2nd recording was

started; MCh: 25 μM methacholine incubated for 15 min + 15 min washout before 2nd recording started; MCh + TTX: 10 min preincubation of 1 μM TTX then application of 25 μM MCh & 1 μM TTX incubated for 15 min + 15 min washout = > 2nd recording started; MCh + LatB: 15 min preincubation of 10 μM latrunculin B then application of 25 μM MCh & 10 μM LatB incubated for 15 min + washout in the presence of LatB + 15 min incubation in ACSF = > 2nd recording started; Jasp: 10 μM jasplakinolide incubated for 20 min = > 2nd recording. Drugs were purchased from Abcam (TTX), Bio-Connect (latrunculin B), Sigma (Methacholine, NMDA), Tocris (APV, CK-666, DHPG, jasplakinolide, MNI-Glutamate, Picrotoxin, PP2).

Live-cell imaging

Spinning-disk confocal microscopy was performed on an inverted Nikon Eclipse Ti with a Perfect Focus System. Glutamate uncaging experiments were imaged with a S Fluor 100 × , 0.5–1.3 NA oil, all other neuron cultures with Plan Fluor 40 × , 1.3 NA oil-immersion objective; slice cultures with a CFI Apo Lambda S LWD 40 × , 1.15 NA water-immersion objective (all Nikon). The Yokogawa spinning disk confocal scanning unit (CSU-X1-A1NeE) is equipped with a triple-band dichroic mirror (z405/488/568trans-pc; Chroma) and a filter wheel (CSU-X1-FW-06P-01; Yokogawa) containing ET-BFP2 (49021), ET-GFP (49002), ET-mCherry (49008) emission filters from Chroma. Excitation is based on Vortran Stradus 405 nm (100 mW), Cobolt Calypso 491 nm (100 mW) and Cobolt Jive 561 nm (100 mW) lasers, photoactivation on a Teem Photonics 355 nm Q-switched pulsed laser. The UV laser light is controlled by the Ilas-2 system (Roper Scientific, France) and is tunable in intensity via an AOTF filter. Images were acquired in sequential mode with a Photometrics Evolve 512 EMCCD camera equipped with an additional 2.0 × lens (Edmund Optics) resulting in a final resolution of 66 nm/pixel. Neuron and slice cultures were imaged in the type 1 Ludin chamber (LIS, Switzerland), positioned in a Tokai Hit Stage Top Incubator (INUBG2E-ZILCS), which is mounted on a ASI motorized stage MS-2000-XYZ enabling multi-position imaging. Slice cultures were positioned upside down on an empty coverslip and kept in place by a ring of platinum laying on the edge of the FHLC membrane patch. The camera, lasers and all motorized parts are controlled by MetaMorph software.

Imaging of microtubule entries in spines and actin dynamics was performed with following parameters. Neuron cultures were imaged in full conditioned medium at 37°C and 5% CO_2 with 5 s intervals and z stacks of 0.7 μm step sizes (4-7 depending on the z orientation of the dendrite). Slices were recorded with the same settings except for a continuous perfusion with ACSF (oxygenated with 95% O_2, 5% CO_2).

For local NMDA applications, dissociated neurons were silenced with 1 μM TTX for 14-18 hr prior recording. MT+TIP comets were recorded for 4 min at 5 s intervals and mTagRFP only every 5th frame in the original culture medium. Puff-applications of 10 mM NMDA through a patch pipette were applied for 2x 50 ms (with a 10 s break) using a Picospritzer III (Parker). The second imaging session was started 1 min after application with the same settings as in the first recording.

Single photon glutamate uncaging of neuron cultures was performed in modified Tyrod's buffer composed of 119 mM NaCl, 5 mM KCl, 2 mM $CaCl_2$, 10 mM HEPES, 10 mM glucose, 1 μM TTX; pH 7.25 and osmolarity of 0.265 mOsm. MNI-glutamate was added in 100 μL buffer to the darkened recording chamber on the microscope stage to a final concentration of 0.5 mM. Uncaging regions were defined as lines with about 2 μm in length and a distance of 1-1.5 μm to the spine head. The stimulation time-lapse recording contained several time points before and after the uncaging session, in which images were taken in 2 s intervals with 4 × 0.8 μm z stacks. The 355 nm uncaging pulse (0.5 Hz for 1 min) lasted for 3-4 ms and preceded the recording of mTagRFP/GCaMP6. The laser power was adjusted to activate around 30% of the imaged spines, except for the uncaging experiments in combination with Cortactin knockdown (Figures 4I and 4J), where a slightly stronger activation stimulus was used. The subsequent imaging of MT+TIP and mTagRFP/GCaMP6 was recorded at 5 s intervals with the same stack size as before.

We want to point out that successive imaging of different neurons/dendrites on the same coverslip sometimes varied in the cellular response to the uncaging stimulus (based on mTagRFP/GCaMP6 readout). We believe that this most likely represent artifacts of the single-photon uncaging, as for instance light scattering by optical dense structures in the light path. For this reason, suspicious recordings with unusual mTagRFP/GCaMP6 dynamics were excluded from the quantification of microtubule dynamics. The intensity of the uncaging laser is sufficient to bleach mTagRFP signals within a few frames if the uncaging region is directly targeted on the spine head (data not shown). Since we never observed spine bleaching in our uncaging experiments, we conclude together with our control experiments in Figure 3C that the observed morphological changes of spines were not an artifact of light stress. The dependence on NMDA receptor activation was tested by uncaging glutamate in the presence of 150 μM DL-2-amino-5-phosphonopentanoic acid (APV).

Super resolution imaging

For dSTORM imaging of lentiviral infected neurons expressing Lifact-TagRFP-Myc, DIV18+ neurons were fixed with 4% PFA. After fixation cells were washed and permeabilized with 0.25% triton-X in PBS. After 3 washes the samples were blocked for 1 hr at RT in PBS with 2% BSA, 0.2% gelatin, 10mM glycin, 50mM NH_4Cl; pH 7.4. Cells were incubated overnight at 4°C with a combination of two mouse anti-myc primary antibodies (Santa Cruz; 9E10 and Oncogene; AB-1 both diluted 1:400). After three more washes in PBS the cells were incubated with secondary anti-mouse Alexa647 for 1 hr at room temperature and washed 3 more times. Super resolution imaging was performed in buffer optimal for Alexa647 as described before [42, 43].

To perform super resolution of actin by transient binding of diffusing Lifeact-GFP [33] or Lifeact-mNeonGreen, cells were first extracted in 0.35% triton-x and 0.15% glutaraldehyde in CB (10 mM MES, 150 mM NaCl, 5mM $MgCl_2$, 5mM EGTA, 5mM Glucose; pH 6.1) for 1 min at 37 degrees. Cells were fixed in 4% PFA in CB at 37°C, washed 3 times and blocked in 3%

BSA for 30 min. To visualize regions for imaging, cells were mildly stained with Phalloidin 568 (Life Technologies, 1/1000). After 3 thorough washes in PBS cells were mounted in PBS supplemented with low concentrations of Lifeact-GFP or Lifeact-mNeonGreen. In this way, transient single molecule binding could be observed with 60-100 ms exposure time. For 2 color-imaging of actin and cortactin, cells transfected with Cortactin-dsRed were fixed, blocked and stained with anti-RFP (1:400, rabbit, Rockland, 600-401-379) overnight at 4°C. Next, neurons were washed 3x in PBS and stained with secondary anti-rabbit-D2 (Ultivue). After 3 more washes coverslips were mounted and supplemented with Lifeact-mNeonGreen and I2-560 imager strand (Ultivue) so that single molecule binding events could be observed with 60-100 ms exposure. Regions of interest could be identified based on the dsRed signal of cortactin. Images were reconstructed using DoM Utrecht (Detection of Molecules, https://github.com/ekatrukha/DoM_Utrecht) [39].

Image analysis and quantification

Image processing

The four dimensional time-lapse data was reduced in complexity by generating average z stack projections before additional image processing and quantifications were performed in FIJI. Time-lapse recordings were corrected for *x-y* drifts using the MultiStackReg plugin whenever required. Curved dendrites in Figures 1J, 3D, and 3I and Video S2 were straightened because of space limitations or for better illustration using the FIJI "Straighten" plugin.

Quantification of microtubule spine entries

Time-lapse recordings of MT+TIP comets were processed with a moving average subtraction and additional low pass filtering to amplify comet signals [36]. Spine entries were manually identified based on maximum intensity projections of the processed data and visually confirmed in the videos. Spine entry frequency is presented as "Spine entries / spine / hour" in order to compensate for variations in recording time and spine density between dendrites. Multiple targeting of the same spine within short time intervals is often caused by alternating catastrophe and rescue events of the same microtubule. Because we here rather focused on the microtubule targeting mechanism than on the functional consequences for the spines, we counted multiple spine targeting as a single event if the imaging data did not clearly confirm independent microtubules as the source of multiple invasions.

Quantification of MT+TIP comet properties

Kymographs were generated from average subtracted and low pass filtered MT+TIP recordings using the FIJI "KymoResliceWide" plugin. The FIJI "Cell Counter" plugin was used to label the start and end points of individual microtubule traces. All coordinates were exported to MATLAB and used to calculate microtubule density, orientation and length. It is important to state that a substantial proportion of microtubule traces crossed the observation limits in space or time. Therefore, our analysis underestimates the actual length of some of the microtubule traces before entering a spine, which should be kept in mind for a correct interpretation of the results presented in Figures 1E and 1H.

Correlation study of spine entries and catastrophes

Time-lapse recordings were processed as in the previous section with the exception that curved dendrites were additionally straightened using the corresponding function in FIJI. All endings of microtubule traces in the kymograph were visually verified in the videos for coincidental spine entries.

Spine size changes following glutamate uncaging

Recordings of mTagRFP were bleach corrected (exponential fit method) and thresholded (percentile method) using corresponding FIJI plugins. ROIs were defined around the heads of activated and distant non-activated spines. Areas corresponding to the spine head sizes were quantified over time using the "Analyze Particles" function. Data was normalized to the average spine size of the first 10 time points representing baseline conditions.

Spine head and base actin quantifications

Mean intensities of the Lifeact signals over time were quantified in manually defined regions of interest (ROI) at the spine base and head. Resulting mean intensities were adjusted for bleaching based on the mean Lifeact signals of the full image over time and then normalized to the first time point in the time-lapse. The graph in Figures 5B and 5C presents averaged signals from 10 s intervals (5 time points) for a better visual arrangement, while Figure S3C shows the raw data of all quantified ROIs.

Visualization of actin and MT+TIP signals at the spine base/neck

ROIs covering the spine base (Lifeact) or spine base and neck (MT+TIP) of the same spine were defined and mean intensities quantified (scheme in Figure 5F). The same method for bleach correction and normalization was used for both channels as described in the previous section. Peaks in the MT+TIP intensities were rechecked in the time-lapse recordings whether they represent spine entries or passing microtubule comets.

Correlation of actin dynamics at the spine base with MT entries

Moving average subtraction and low pass filtering were applied to the MT+TIP recordings to improve comet signals. Spine entries were identified by the maximum intensity projections of the improved time lapses. Using the MT comets trajectory and the position of the spine head and neck structures, we verified that the recorded z stack included the presumed position of the spine base within the dendrite. We further excluded dendritic sections with high spine densities that did not allow to clearly identifying the spine base of an individual spine. In combination, this excluded a considerable number of spine targeting events for this analysis. In 21 dendrites we found 43 spines being targeted by microtubules which met the above criteria. Next, we visually inspected the corresponding spine base for increased actin dynamics within a time window of 1 min before the microtubule entered the spine.

As control we analyzed all 540 spines of the 21 dendrites for comparable actin dynamics at the spine base. For each dendrite we choose the time point of a spine invasion and analyzed for 1 min in reverse.

QUANTIFICATION AND STATISTICAL ANALYSIS

Data processing, statistical analysis and diagrams were done in Excel and Prism (GraphPad) software. The assumption of normality was tested with D'Agostino-Pearson omnibus normality test. All statistical details of experiments, including the definitions, exact values of n, and statistical tests performed, can be found in the corresponding figure legends. The experiments were independently repeated three or more times to ensure consistency and reproducibility. No specific strategy for randomization and/or stratification was employed. The studies were blind in data analysis. No samples were excluded from analysis if not stated explicitly in the corresponding analysis section.